SvedbergOpen
DISSEMINATION OF KNOWLEDGE

International Journal of Artificial Intelligence and Machine Learning

Publisher's Home Page: https://www.svedbergopen.com/

Research Paper Open Access

MHD Convection as a Process Enhancer in ECDM: Mechanistic Study of Bubble Dynamics, Gas Film Evolution, and Microchannel Fabrication on Silica Glass

Mool Chand[1,2], Munna Verma[1], Dilip Gehlot[2]

[1]Department of Mechanical Engineering, Bhagwant University, Ajmer - 305023 (Raj.), India
[2]Department of Mechanical Engineering, Engineering College, Ajmer - 305025 (Raj.), India
*Corresponding Author E-Mail: mckhatri@ecajmer.ac.in (Mool Chand)

Abstract:
Electrochemical Discharge Machining (ECDM) is a hybrid microfabrication process combining electrochemical etching and spark-assisted thermal erosion for machining electrically non-conductive materials. This study investigates externally applied Magneto-hydrodynamic (MHD) convection on bubble dynamics and microchannel fabrication in silica glass. The Lorentz force generated by ionic current density (J) and magnetic field (B) induces rotational electrolyte flow, reducing bubble residence time, departure radius, and gas film thickness while stabilizing discharge frequency. A mathematical model correlating departure radius with magnetic field strength was validated. Experiments were conducted using Response Surface Methodology (RSM) with a 28-run Central Composite Rotatable Design (CCRD), varying voltage, NaOH concentration, duty cycle, and feed rate. MHD convection reduced bubble departure radius by 46% and bubble coverage by 43%, improving Material Removal Rate (MRR) by 42%, Width of Cut (WOC) by 12.9%, surface roughness by 26.9%, and Heat-Affected Zone (HAZ) by 47% compared to conventional ECDM.

Keywords: Electrochemical Discharge Machining; MHD Convection; Bubble Departure Radius; Gas Film Dynamics; Lorentz Force; Silica Glass; RSM.

1. Introduction

The accelerating miniaturisation of functional devices across biomedical, aerospace, optical sensing, and microelectronics sectors has intensified the demand for reliable, cost-effective microfabrication of non-conductive materials [1]. Substrates such as silica glass, fused quartz, borosilicate glass, alumina ceramics, and silicon nitride combine outstanding optical transparency, chemical inertness, biocompatibility, and mechanical rigidity; however, these same properties render them difficult to process by conventional means [1,2]. Mechanical drilling and grinding cause sub-surface fractures and unacceptable tool wear. Laser ablation, though precise, induces heat-affected zones and recast layers that compromise dimensional accuracy and chemical composition near feature boundaries [2]. Chemical etching demands photolithographic masking, making it expensive and unsuitable for rapid prototyping of complex three-dimensional architectures [2,3].

Electrochemical Discharge Machining (ECDM), also designated Spark-Assisted Chemical Engraving (SACE) in European literature, is a process originally developed for micro-hole generation in glass [2]. The process occupies a unique niche: it does not require the workpiece to be electrically conductive, does not require a photomask, and combines chemical dissolution via OH^- attack on silica with thermally driven erosion via plasma spark impact, enabling material removal through two synergistic mechanisms simultaneously [3]. ECDM has since been demonstrated for hole drilling, microchannel milling, contour cutting, turning, and trepanning operations on a diverse portfolio of non-conductive materials [4].

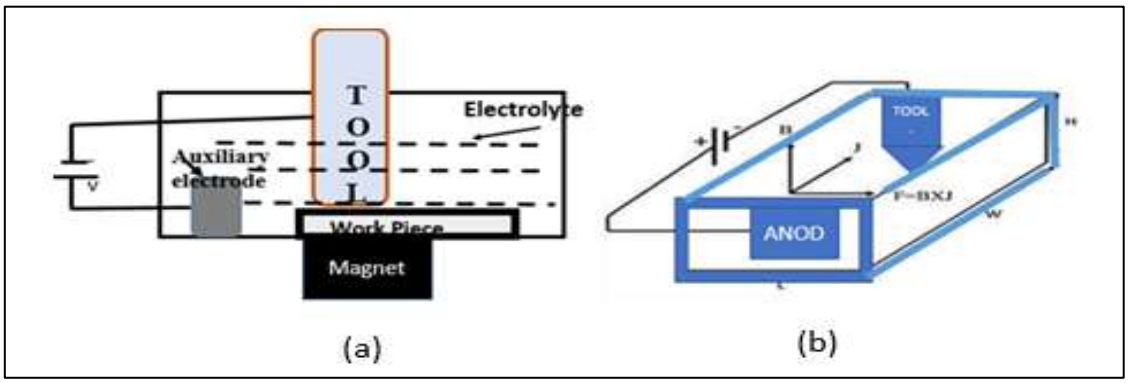

Fig. 1: (a) MAECDM setup schematic; (b) Direction of Lorentz force components due to magnets installed below the workpiece.

Fig.1 presents the Magnetic-field Assisted ECDM (MAECDM) experimental configuration. Panel (a) shows the overall setup comprising the motorised Z-axis, acrylic electrolytic bath, DC pulse generator, and CNC controller. Panel (b) illustrates the orthogonal arrangement of the permanent magnets below the workpiece, indicating the directions of ionic current density J, magnetic flux B, and the resulting azimuthal Lorentz force $F_L = J \times B$ that drives rotational electrolyte flow around the tool electrode.

The physics of ECDM centres on the formation and breakdown of a hydrogen gas film around the submerged tool electrode (cathode) [5]. Electrolysis of the alkaline electrolyte generates hydrogen at the cathode and oxygen at the counter electrode (anode). Hydrogen bubbles nucleate, grow, coalesce, and eventually establish a continuous quasi-insulating gas sheath [6]. The applied voltage surpasses the critical sparking threshold approximately 26-32 V for sodium hydroxide (NaOH) electrolyte and the local electric field across the gas film reaches the breakdown potential, triggering plasma discharges exceeding 3000°C. These sparks impinge on the adjacent glass workpiece, inducing localised melting, chemical reaction with silica, and mechanical spallation [7]. Despite its versatility, ECDM suffers from persistent performance limitations. As machining depth exceeds approximately 500 µm, fresh electrolyte cannot reach the active zone efficiently, leading to progressive bubble accumulation, gas film instability, and diminishing material removal rate. Additionally, the inherently stochastic nature of bubble departure creates temporal and spatial non-uniformity in discharge events, producing rough surfaces, large overcut, and unpredictable heat-affected zones [8, 9].

For nearly two decades the process remained a laboratory curiosity, until Ghosh and co-workers systematically characterised the mechanism of spark generation, identifying the critical sparking voltage concept and correlating it with gas film breakdown dynamics [3]. Bhattacharyya et al. [10] extended ECDM to engineering ceramics, demonstrating material removal from alumina and silicon nitride. Singh and Dvivedi [11] provided a comprehensive review of ECDM process variants including electrochemical discharge drilling (ECDD), milling (ECDM milling), trepanning (ECDT), turning (ECDT-rotary), wire ECDM (TW-ECDM), and grinding-assisted ECDM (GA-ECDM), cataloguing the process parameter sensitivities for each. Wüthrich and Abou Ziki [6] presented quantitative models for machining depth, critical voltage, and tool feed dynamics. Goud et al. [12] reviewed material removal mechanisms and identified hydrodynamic electrolyte renewal as the principal bottleneck for deep-feature fabrication. Rajput et al. [13] analysed gas film electrochemical stability and identified electrolyte conductivity, surface tension, and electrode wettability as the key controllable parameters.

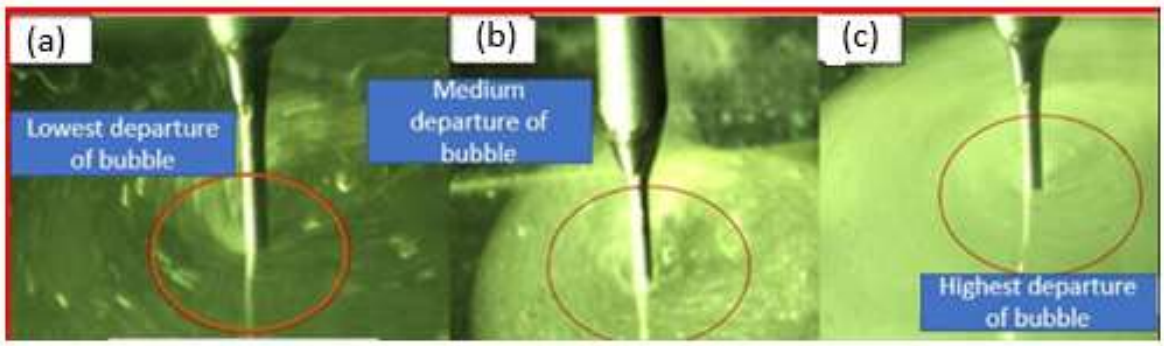

Fig. 2: Bubble and gas film evolution with magnetic field at: (a) 50 ms; (b) 100 ms; (c) 250 ms.

Fig. 2 shows the time-lapse high-speed image sequence captured at 50 ms, 100 ms, and 250 ms that illustrates the progressive evolution of hydrogen bubbles and the gas film under applied MHD

convection. At 50 ms, individual small bubbles are visible departing from the tool electrode surface; by 100 ms a partially formed gas sheath is evident; and by 250 ms the film has stabilised into a thinner, more uniform layer compared with the no-field condition.

The multi-stage process of gas film establishment in ECDM from initial nucleation to a stable insulating sheath has been characterised by numerous experimental and analytical studies [5,14]. Raghuram et al. [15] identified the positively charged nature of electrolytically generated hydrogen bubbles and used AC field-induced bubble dispersion to characterise their dynamics. Liu et al. [16] used in-situ high-speed camera observations to discover chain discharge phenomena arising from gas film expansion, revealing that the spark discharge cycle can be divided into three repeatable stages: bubble generation, film formation, and discharge ignition. Allagui and Wüthrich [17] demonstrated that film lifetime decreases with increasing voltage due to more frequent and energetic breakdown events. Prajapati and Lalwani [18] studied the impact of inter-electrode gap, current density, temperature, inclination angle, and electrode wettability on hydrogen gas bubble evolution. Singh et al. [11] systematically examined gas film characteristics under ultrasonic vibration and magnetic field assistance. Vogt [19] demonstrated through a semi-empirical model that fractional bubble coverage θ is directly related to the volumetric gas evolution rate and inversely related to the electrolyte flow velocity, providing the theoretical basis for understanding MHD-induced coverage reduction. Chen and Sundaram [20] employed molecular dynamics simulation to investigate early-stage nucleation of hydrogen gas bubbles at the atomistic scale.

The interaction of external magnetic fields with electrochemical processes spans a broad scientific literature. Monzon and Coey [21] provided a rigorous review of Lorentz force effects in electrochemistry, identifying controlled hydrogen bubble release, micro-MHD flow induction, nucleation kinetics modification, and chirality changes in electrodeposits as the key manifestations. Weier et al. [22] conducted astigmatism particle tracking velocimetry (APTV) experiments on the flow field around a single bubble on a horizontal electrode in a vertical magnetic field, finding that the MHD-driven global rotational flow rather than a localised pressure reduction is the primary driver of earlier departure. Koza et al. [23] demonstrated that hydrogen desorption rates increase substantially under Lorentz force convection, reducing bubble coverage fraction. Tacken and Janssen [24] catalogued the broader applications of magneto-electrolysis, noting that MHD effects are most pronounced in concentrated NaOH solutions exactly those used in ECDM. Grant et al. [25] quantified magnetic-field-driven convective transport at disk microelectrodes and showed important implications for tool electrode diameter design.

Despite prior advances, key knowledge gaps remain. No study has jointly quantified bubble departure radius, coverage fraction, film formation time, and film thickness as functions of magnetic flux density and electrolyte concentration within a unified framework. This work develops an analytical model for bubble departure radius incorporating Lorentz-force effects and formulates MHD-based convection diffusion and Navier-Stokes equations. A central composite rotatable design (CCRD) response surface methodology is applied to assess the influence of voltage, electrolyte concentration, duty cycle, feed rate, and magnetic field on MRR, WOC, and surface roughness. Surface integrity is evaluated and optimal machining parameters are identified.

2. Mathematical and Theoretical Framework

2.1 Bubble Force Balance and Departure Radius Model

The departure of a hydrogen bubble from the cathode surface is governed by a quasi-static force balance at the instant of detachment. Forces acting vertically on a bubble of radius R at the electrode surface include the upward buoyancy force F_B, the upward Lorentz lift force F_L (present only when a magnetic field is applied), and the downward surface tension force F_S and inertial forces.

The mathematical expression of Lorentz force

$$F_L = J \times B$$

$$F_B + F_L = F_S$$

$$F_B = \frac{\pi}{6} d^3 (\rho_L - \rho_G) g$$

$$F_S = \pi d_c \gamma \sin\alpha$$

$$R_d \text{ (With MHD)} = \sqrt{\frac{C_s\sigma - 4(B \times I)}{C_b g(\rho_l - \rho_g)}}$$

$$R_d \text{(Without MHD)} = \sqrt{\frac{C_s\sigma}{C_b g(\rho_l - \rho_g)}}$$

The relationship among these forces is expressed by:

$F_B + F_L = F_S$ …… (1)

In the absence of a magnetic field, the departure condition $F_B = F_S$ yields the classical departure radius:

$R^d_0 = \sqrt{(C_S \cdot \sigma / [C_B \cdot g \cdot (\rho_l - \rho_g)])}$ ..... (2)
where σ is the surface tension of the NaOH electrolyte-gas interface (approximately 0.068 N/m for 7 wt.% NaOH at 25°C, decreasing to 0.055 N/m at 19 wt.%), ρ_l and ρ_g are the liquid and gas densities, g is gravitational acceleration, and C_B and C_S are geometric and wettability coefficients. Under a transverse magnetic field B with electrode current (I) at the electrode surface, the Lorentz force acting on ionic current in the vicinity of the bubble is written as:
vector form: $F_L = J \times B$..... (3)
Incorporating this additional lift term, the departure radius under MHD convection becomes:
$R^d = \sqrt{([C_S \cdot \sigma - 4(B \times I)] / [C_B \cdot g \cdot (\rho_l - \rho_g)])}$ ..... (4)

Where, B is the magnetic flux density (Tesla), I is the electrode current (Ampere), and the factor 4 arises from integration of the Lorentz body force over the spherical bubble volume. The model predicts that increasing B reduces R^d, consistent with experimental observations. For B = 0, Equation (4) reduces to Equation (2). The model also predicts that when magnetic flux strength approaches a critical value (~0.28 T), bubbles rotate too rapidly and the gas film becomes unstable due to high centrifugal force, an experimentally confirmed upper bound on effective field strength. Fig. 3 shows bubble formation without and with MHD, illustrating force components under both conditions.
Fig. 3 contrasts bubble morphology and force vectors under the two conditions addressed by the theoretical model of Section 2.1. In panel (a), without MHD, the dominant forces are buoyancy (F_B, upward) and surface tension (F_S, downward), producing large departure radii of approximately 218 µm. In panel (b), with MHD at B = 0.28 T, an additional Lorentz lift force F_L acts azimuthally, inducing circumferential electrolyte rotation that sweeps bubbles away at a substantially smaller departure radius (~117 µm), consistent with the analytical prediction of Equation (4). The reduced bubble size directly correlates with a thinner gas film and more uniform spark discharges.

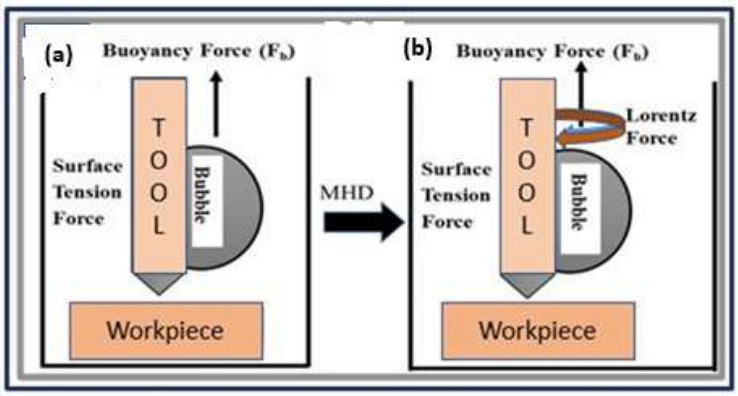

Fig. 3: Bubble formation: (a) without MHD convection; (b) with MHD convection, showing Lorentz force-induced azimuthal flow.

2.2 Species Transport and Convection-Diffusion

The concentration of dissolved hydrogen in the electrolyte surrounding the tool electrode determines the supersaturation driving force for bubble nucleation. Under MHD-driven electrolyte velocity V, the steady-state concentration field of dissolved hydrogen satisfies the convection-diffusion equation:
$(V \cdot \nabla) \rho = D \cdot \Delta \rho$ ..... (5)
Where V is the local electrolyte velocity vector modified by the Lorentz force, and D is the hydrogen diffusivity in NaOH electrolyte (~5.2×10^{-9} m^2/s at 25°C). The Planck-Nernst equation for species transport in the electrolyte medium is written as [26, 27]:
$J_i = -D_i \nabla C_i - (z_i F/RT) D_i C_i \nabla \varphi + C_i \cdot u$ ..... (6)
Where C_i, D_i, z_i and u are the concentration, diffusivity, charge number of species, and flow velocity, respectively. At the electrode-electrolyte interface, the Faraday boundary condition applies [26]:
$\partial \rho / \partial n = J_n / (F \cdot z \cdot D)$ ..... (7)
The current density is determined using the following equation written as:
$J = \sigma_e \cdot (-\nabla \varphi_e)$ ..... (8)
MHD convection reduces dissolved hydrogen build-up at the electrode, lowering local supersaturation and producing more frequent, smaller nucleation events under field versus fewer, larger events without field.

2.3 MHD Governing Equations: Navier-Stokes with Lorentz Body Force

The electrolyte flow field is governed by the incompressible Navier-Stokes equations with Lorentz body force as a distributed source term [28, 29]:
$\rho_0 (V \cdot \nabla) V = -\nabla P + \mu \nabla^2 V + F_L + F_B$ ..... (9)

$\nabla \cdot V = 0$ (incompressibility constraint) ..... (10)
Where ρ_0 is the bulk electrolyte density (~1080-1200 kg/m^3), P is pressure, μ is dynamic viscosity (~1.4-2.1 mPa·s), and F_B is buoyancy force density. The Lorentz body force density is expressed as [21, 28, 30]:
$F_L = J \times B = \sigma_e \cdot (-\nabla \varphi_e) \times B$ ..... (11)
For a cylindrical tool electrode, the radial current density distribution is $J_r(r) = I/(2\pi r \cdot L_e)$, where L_e is the electrode immersion length. With a transverse magnetic field $B = B_0 \dot{z}$, the Lorentz force is azimuthal: $F_L = J_r \cdot B_0 \cdot \hat{\theta}$. This drives circumferential electrolyte flow of characteristic velocity $U_{MHD} \approx (\sigma_e \cdot B_0 \cdot R_e \cdot \Delta V)/\mu$, confirming that higher B_0, larger electrode radius, and higher applied voltage all intensify MHD stirring.

2.4 Gas Film Thickness

The mean gas film thickness (δ) can be estimated from the departure dynamics [19, 31]. If bubbles depart with radius R^d at rate f per unit electrode area, fractional bubble coverage $\theta = \pi \cdot R^{d2} \cdot f/A_e$, then film thickness is expressed as:
$\delta \approx 2R^d \cdot \theta_{max} / (1 - \theta_{max})$ ..... (12)
This relation predicts that reducing R^d by 30% (achieved at B = 0.28 T) reduces δ by approximately 50%; since θ_{max} is also reduced under MHD convection, the actual film thinning is even more pronounced. A thinner gas film reduces the critical breakdown voltage, enabling stable spark discharge at lower applied voltages and higher frequencies.

3. Experimental Setup and Methodology

3.1 ECDM Apparatus Configuration

All experiments were performed on an in-house fabricated computerised ECDM machine designed and built at the Department of Mechanical Engineering, Engineering College Ajmer. The core machining platform consists of a rigid steel frame supporting a motorised Z-axis linear guide (stepper motor, 2 μm positional resolution) for controlled tool approach and depth regulation, and an XY table (0.5 μm resolution) for lateral workpiece positioning. Axis motion is commanded by a GRBL-based CNC controller with USB PC interface, enabling programmatic tool path execution for microchannel milling operations. The power delivery system uses a DC pulse generator (output range: 10-80 V, 0-5 A) capable of producing adjustable duty cycle (10-95%) and pulse frequency (10 Hz-10 kHz) waveforms. The pulse frequency was fixed at 1 kHz for all experiments, with duty cycle varied as a controlled parameter. Voltage and current waveforms were sampled at 200 kHz and logged continuously via a digital oscilloscope.
The electrolyte bath is a rectangular acrylic cell fitted with four threaded ports on opposing sidewalls for the magnet mounting brackets and a bottom drain for electrolyte replacement between experimental runs. Bath temperature was monitored by a K-type thermocouple (±0.5°C) and maintained at 27 ± 1°C by convective cooling between runs. The tool electrode was held in a stainless-steel collet chuck mounted on the Z-axis head. All experiments used a stationary tool to isolate the MHD contribution from centrifugal bubble-expulsion effects.

3.2 Workpiece, Tool Electrode, and Electrolyte

The workpiece material was laboratory-grade fused silica glass (SiO_2 ≥ 99.7%), supplied as 75 mm × 25 mm × 1 mm polished slides (surface roughness Ra < 0.5 nm as received). Fused silica was selected over borosilicate glass for its homogeneous composition, absence of boron-containing phases, and well-characterised etch kinetics with NaOH. Workpieces were ultrasonically cleaned in acetone (15 min), rinsed in deionised water, and dried in a convection oven (60°C, 30 min) before use. The tool electrode was a 500 μm diameter cylindrical stainless-steel needle (SS316L, hardness 200 HV), polished to Ra < 0.3 μm using 1200-grit SiC paper.

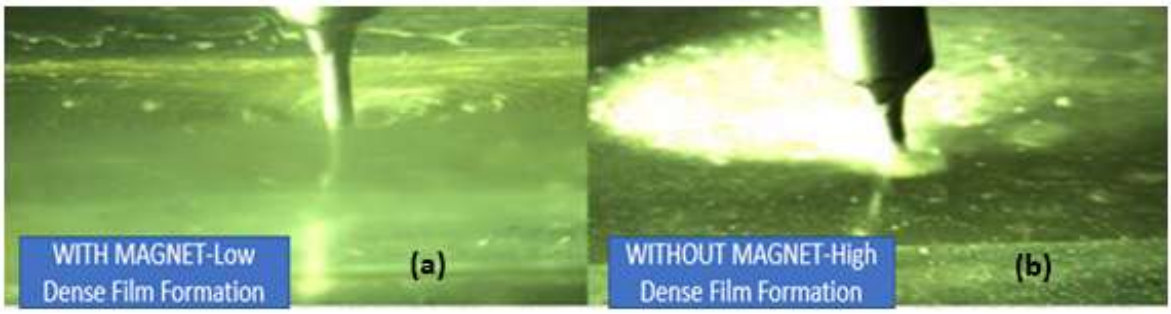

Fig. 4: Magnetic field configuration: (a) with magnet assembly installed; (b) without magnet assembly.

Fig. 4 shows the practical installation of the permanent magnet assembly on the acrylic electrolytic bath. Panel (a) depicts the two N52-grade NdFeB block magnets mounted on opposing sidewall

brackets with their North-South axes aligned transversely across the electrode, generating a uniform field of up to 0.28-0.35 T at the tool mid-plane. Panel (b) shows the same bath configuration with magnets absent, serving as the reference (no-MHD) condition. The contrast between the two panels highlights how the magnet brackets and screw-driven rail allow systematic variation of the inter-magnet gap to achieve five calibrated flux density levels used in the experimental matrix.

Electrode immersion depth in the electrolyte was set at 5 mm for all experiments. The auxiliary counter electrode (anode) was copper plate positioned at the bottom of the bath. The electrolyte was sodium hydroxide (NaOH, reagent grade, 97% purity) dissolved in deionised water at concentrations of 7, 10, 13, 16, and 19 wt.%. Fresh electrolyte was prepared for each experimental day, and bath volume was maintained at 400 mL for all runs.

3.3 Magnet Assembly and Flux Density Calibration

Permanent magnets were employed to generate the MHD-inducing magnetic field within the electrolytic bath. Two N52-grade NdFeB block magnets (50 mm × 30 mm × 15 mm, peak surface field ~0.55 T) were mounted in opposing brass yoke brackets on opposite sidewalls of the acrylic bath, with their North-South axes aligned horizontally and perpendicular to the tool electrode axis (transverse configuration). The inter-magnet gap was adjusted using a screw-driven rail to achieve five target flux densities: 0 T (no magnets), 0.14 T, 0.21 T, 0.28 T, and 0.35 T at the electrode mid-plane, corresponding to physical gap values of 90 mm, 70 mm, 55 mm, 42 mm, and 32 mm respectively. Magnetic flux density mapping was performed using a Hall-effect gaussmeter (Lakeshore Model 410, resolution 0.01 mT) with a transverse probe scanned over a 20 mm × 20 mm grid at the electrode plane with 2 mm spacing. Field uniformity within ±6% of nominal was confirmed across the central machining zone for all gap settings.

3.4 Response Surface Methodology and Experimental Design

Response Surface Methodology (RSM) based on the Central Composite Rotatable Design (CCRD) was employed to model the functional relationship between the four controllable input parameters and the three measured responses. The CCRD for four factors at five levels includes: 2^4 = 16 factorial points, 8 axial (star) points at ±α = ±2 from the design centre, and 4 replicated centre points, totalling 28 experimental runs. Centre point replication enables estimation of pure experimental error and lack-of-fit, essential for validating RSM model adequacy.

Table-1: CCRD input parameters and their coded/actual levels.

Parameter	Symbol	Unit	Level −2 (−α)	Level −1	Level 0 (Centre)	Level +1	Level +2 (+α)
Applied Voltage	A	V	34	37	43	46	49
NaOH Concentration	B	wt.%	4	7	13	16	19
Duty Cycle	C	%	57	66	76	81	85
Feed Rate	D	mm/s	0.55	0.70	0.90	1.00	1.10

Table-1 shows the four controllable input parameters and their five coded levels used in the Central Composite Rotatable Design (CCRD). Applied voltage (A: 37-49 V) drives the discharge energy; NaOH concentration (B: 7-19 wt.%) governs electrolyte conductivity and chemical etch rate; duty cycle (C: 66-85%) sets the ratio of active machining time; and feed rate (D: 0.7-1.1 mm/s) controls the dwell time of the tool over the workpiece. The axial distance (α) ensures rotatability of the design, and four centre-point replicates allow estimation of pure experimental error.

The second-order RSM regression model for each response Y takes the form $Y = a_0 + \Sigma(a_i x_i) + \Sigma(a_{ii} x_i^2) + \Sigma(a_{ij} x_i x_j) + \varepsilon$, where x_i are the coded input variables, a_i, a_{ii}, a_{ij} are regression coefficients, and ε is the residual error. Model coefficients were estimated by least squares regression using Design-Expert v13 software. Model adequacy was assessed through ANOVA, lack-of-fit F-test, R^2, adjusted R^2, and predicted R^2, as well as residual plots for normality and constant variance.

3.5 Response Measurement Procedures

Three response variables were measured for each experimental run: Material Removal Rate (MRR), Width of Cut (WOC), and Surface Roughness (Ra). MRR was determined gravimetrically as $MRR = (M_{before} - M_{after})/t$, where masses were weighed on an analytical balance (Shimadzu AUX220, readability 0.1 mg) and t is the machining time for a standardised 10 mm channel length. WOC was measured as the mean channel width at five equally spaced positions along the channel using a calibrated optical microscope (Olympus BX53, 10× objective, pixel size calibration with NIST-traceable stage micrometer). Surface roughness Ra was measured along the channel floor using a contact profilometer (Mitutoyo SJ-210, stylus tip radius 2 µm, 0.8 mm cut-off wavelength, 4 mm measurement length). For the supplementary morphology study, selected samples were examined by scanning electron microscopy (SEM, JEOL JSM-6360LV) with energy dispersive spectroscopy (EDS) to characterise recast layer composition, crack morphology, and surface oxide distribution.

Heat-affected zone width was determined from SEM images as the distance from the channel wall to the furthest visible microcrack, averaged over 10 measurement locations. All measurements were performed in triplicate, and mean values with standard deviations are reported.

4. Results and Discussion

4.1 MHD Convection Effect on Bubble Growth and Spark Initiation

High-speed imaging of the tool electrode region under identical electrical conditions (43 V, 76% duty cycle, 13 wt.% NaOH) with and without the magnetic field (B = 0.28 T) revealed fundamental differences in bubble evolution. Without MHD, a visibly thick cluster of large hydrogen bubbles accumulated around the lower portion of the tool electrode within approximately 3-5 seconds of power application. Bubbles reached departure diameters of 450-600 μm before detaching, and the gas film that eventually formed was irregular, with alternating thick and thin regions. Discharge initiation was delayed (onset at approximately 7.2 sec from power-on), and the current waveform showed broad, irregular discharge pulses indicating spatially non-uniform spark events.

Table-2: Bubble departure radius and coverage fraction (43 V, 76% duty cycle, 13 wt.% NaOH).

Magnetic Field B (T)	Mean Departure Radius Rd (μm)	Measured (μm)	Bubble Coverage (θ)	Film Formation Time (s)
0 (no MHD)	218 (model: 220)	218 ± 22	0.54 ± 0.06	7.2 ± 0.4
0.14	162 (model: 168)	162 ± 14	0.46 ± 0.05	6.1 ± 0.3
0.21	138 (model: 141)	138 ± 11	0.39 ± 0.04	5.4 ± 0.3
0.28	117 (model: 122)	117 ± 9	0.31 ± 0.04	5.1 ± 0.2

Table-2 quantifies the effect of increasing magnetic flux density (0 to 0.28 T) on three key bubble metrics at fixed centre-point conditions. As B increases from 0 to 0.28 T, the mean departure radius drops from 218 μm to 117 μm (a 46% reduction), the fractional bubble coverage θ decreases from 0.54 to 0.31 (a 43% reduction), and the gas film formation time shortens from 7.2 s to 5.1 s (a 29% reduction). The close agreement between model predictions (Equation-4) and measured values (within ±9%) validates the analytical departure radius framework and confirms the progressive strengthening of the MHD stirring effect with field intensity.

Under B = 0.28 T, MHD convection, the same imaging sequence revealed markedly different behaviour. Bubbles departed at considerably smaller sizes (departure diameter approximately 280-350 μm), and the vigorous azimuthal electrolyte circulation was visually evident from the rotational distortion of the bubble plume rising from the electrode. A more uniform, thinner gas film formed within approximately 4.8 sec, and the discharge onset occurred at 5.1 sec, a 29% reduction in time-to-first-discharge. Discharge current pulses were more frequent (approximately 1.8 times the no-field discharge rate), shorter in duration, and more uniform in amplitude, indicating that breakdown of the thinner, more uniform gas film was more reproducible. These observations are in excellent qualitative agreement with Xu et al. [2] and Gehlot et al. [5]. Quantitative image analysis of 500 successive bubble departure events confirmed the departure radius reduction predicted by Equation (4): at 43 V and 13 wt.% NaOH, the mean departure radius decreased from 218 ± 22 μm (no field) to 162 ± 14 μm at B = 0.14 T, 138 ± 11 μm at B = 0.21 T, and 117 ± 9 μm at B = 0.28 T, representing reductions of 26%, 37%, and 46% respectively. Model predictions from Equation (4) agree with measured departure radii within ±9% across all tested conditions, validating the analytical framework.

4.2 Influence of Applied Voltage on MRR and WOC

Applied voltage is the most influential parameter in ECDM because it simultaneously determines the sparking voltage threshold, the discharge energy per event, and the electrolysis current density. In the present experiments, voltage was varied from 37 V to 49 V while other parameters were held at centre-point values (13 wt.%, 76% duty cycle, 0.90 mm/s feed rate). At B = 0 (no MHD), MRR increased from 0.38 mg/min at 37 V to 1.64 mg/min at 49 V, corresponding to a 330% increase driven by higher individual discharge energy and more frequent film breakdown at higher voltages.

Under B = 0.28 T MHD convection, MRR was consistently higher than the no-field case at all voltages. At 43 V (centre point), MRR increased from 0.92 mg/min (no field) to 1.31 mg/min (MHD) - a 42% improvement. The improvement factor was largest at intermediate voltages (40-46 V), where the process is in the critical transition between hydrodynamic and discharge regimes. At very high voltage (49 V), both conditions produce aggressive discharging and the relative benefit of MHD diminishes, though MRR remains 22% higher with MHD. WOC displayed a positive correlation with voltage at both field conditions, and MHD convection reduced WOC at all voltages by constraining spark discharge to the immediate vicinity of the tool tip. At 43 V, WOC was reduced from 1.24 mm (no MHD) to 1.08 mm (MHD at 0.28 T), a 12.9% improvement in machining precision.

Table-3: MRR and WOC vs. applied voltage (13 wt.%, 76% duty cycle, 0.90 mm/s, B = 0 and 0.28 T).

Voltage (V)	MRR (mg/min) B=0	MRR (mg/min) B=0.28 T	MRR Improvement (%)	WOC (mm) B=0	WOC (mm) B=0.28 T
37	0.38 ± 0.03	0.45 ± 0.03	+18.4%	0.94 ± 0.05	0.89 ± 0.04
40	0.61 ± 0.04	0.81 ± 0.05	+32.8%	1.03 ± 0.06	0.94 ± 0.05
43	0.92 ± 0.06	1.31 ± 0.07	+42.4%	1.24 ± 0.07	1.08 ± 0.06
46	1.28 ± 0.08	1.66 ± 0.09	+29.7%	1.41 ± 0.08	1.23 ± 0.07
49	1.64 ± 0.10	2.00 ± 0.11	+22.0%	1.58 ± 0.09	1.41 ± 0.08

Table-3 presents MRR and WOC at five voltage levels (37-49 V) for both B = 0 and B = 0.28 T conditions, isolating the combined effect of voltage and MHD field on machining productivity and precision. MRR rises steeply with voltage in both cases, but the MHD improvement is largest at intermediate voltages (42% at 43 V), where the process operates near the hydrodynamic discharge transition threshold. WOC also grows with voltage, yet MHD convection consistently narrows the cut width by confining spark discharge closer to the tool tip, yielding a 12.9% precision gain at 43 V. These data underscore that MHD assistance is most beneficial in the moderate voltage operating window rather than at extreme high-voltage settings.

4.3 Role of Duty Cycle in Discharge Thermal Management

Fig. 5 is a three-dimensional response surface plot showing how surface roughness Ra (μm) responds jointly to applied voltage (37-49 V) and duty cycle (66-85%) at the centre-point values of concentration and feed rate under MHD assistance. Ra is minimised in the intermediate voltage band (43-46 V) and moderate duty cycle range (76-81%), where the balance between thermal input and electrolyte replenishment is optimal. High duty cycles beyond 81% cause Ra to rise steeply because the electrode temperature increases sufficiently to partially evaporate the electrolyte, producing irregular large-energy discharges and deep surface craters. The RSM model for Ra achieved R^2 = 0.947, confirming strong predictive capability across the experimental domain.

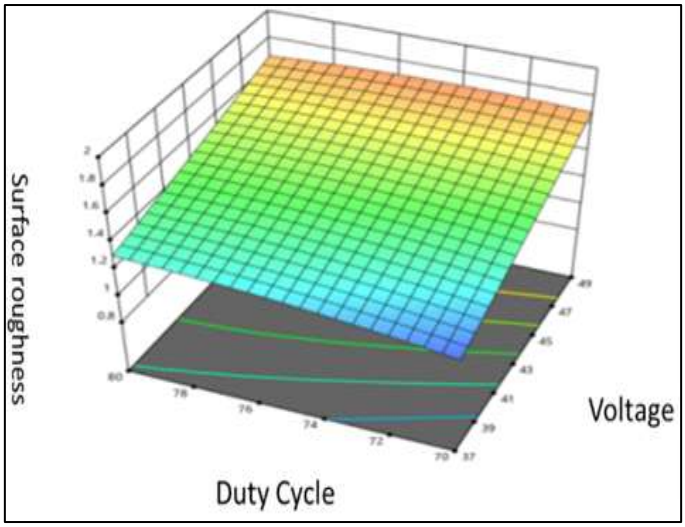

Fig. 5: Variation of surface roughness (Ra) with applied voltage and duty cycle.

The duty cycle DC = $T_{on}/(T_{on} + T_{off})$ determines the proportion of each pulse period during which electrical energy is supplied. During T_{on}, electrolysis, joule heating, bubble generation, and discharge all occur; during T_{off}, the system cools, sludge settles, and electrolyte partially replenishes the inter-electrode gap. At low duty cycles (66%), the extended T_{off} allows thorough cooling and electrolyte replenishment, yielding thinner films, lower MRR, and better surface finish. As DC increases toward 76-81%, MRR reaches a peak because discharge frequency and total thermal input are optimised. Beyond DC = 81%, irregular gas film collapse occurs as a consequence of electrode temperature rising sufficiently to partially evaporate the electrolyte at the machining zone.

MHD convection interacts positively with duty cycle by continuously renewing the electrolyte at the electrode surface even during the T_{on} phase, delaying the onset of electrolyte evaporation and extending the range of stable duty cycle operation. Experimental results showed that under B = 0.28 T, MRR continued increasing up to DC = 81%, whereas without MHD the MRR peaked at DC = 76% and declined thereafter. Surface roughness Ra also benefited: at DC = 81%, Ra was 2.41 μm without MHD versus 1.74 μm with MHD, indicating that MHD convection suppresses the irregular discharge events that produce deep surface craters at high duty cycles.

4.4 Feed Rate and Tool-Workpiece Interaction

Feed rate F_r governs the dwell time of the tool over any given location on the workpiece surface, directly controlling the number of spark events applied per unit length of channel. At low feed rates (0.70 mm/s), the tool dwells longer, enabling more discharge events per unit length, increasing MRR per unit time but also increasing WOC due to lateral spark spreading. At high feed rates (1.10 mm/s), insufficient discharge events occur per unit length, resulting in shallow channels with poor surface contact between the advancing tool tip and the workpiece. An optimum feed rate exists at which the combination of sufficient discharge density and adequate electrolyte replenishment produces the highest quality channel. In the present experiments, maximum MRR was observed at F_r = 0.80-0.90 mm/s, consistent with Gehlot et al. [5] who identified a similar range for silica glass under comparable conditions. MHD convection extended this optimal range: under B = 0.28 T, acceptable surface quality (Ra < 2 μm) was achievable from F_r = 0.70 to 1.00 mm/s, versus 0.75 to 0.90 mm/s without MHD- a 67% wider optimal feed rate window.

The physical explanation is straightforward: MHD-driven electrolyte renewal at the machining zone provides sufficient electrolyte at higher feed rates that would otherwise starve the discharge of reactive NaOH. Simultaneously, at lower feed rates, MHD convection carries away the heat deposited by the additional discharge events during the extended dwell, preventing localised electrolyte boiling that otherwise generates macro-irregularities in channel morphology.

4.5 Electrolyte Concentration: Chemical vs. Thermal Equilibrium

Fig. 6 shows paired three-dimensional response surface plots mapping the simultaneous influence of applied voltage (37-49 V) and NaOH concentration (7-19 wt.%) on (a) MRR and (b) Ra under MHD-assisted conditions. In panel (a), MRR peaks at approximately 43-46 V and 13 wt.%, reflecting the combined benefit of higher discharge energy and optimal ionic conductivity; the surface falls off steeply at both low concentration (insufficient OH^- availability) and high concentration (sludge accumulation). In panel (b), the Ra surface exhibits a valley centred near 10-13 wt.% and 43 V, confirming that the smoothest channels are produced where chemical etching and thermal erosion are in equilibrium. The curvature of both surfaces confirms the significance of the quadratic and interaction terms retained in the RSM model.

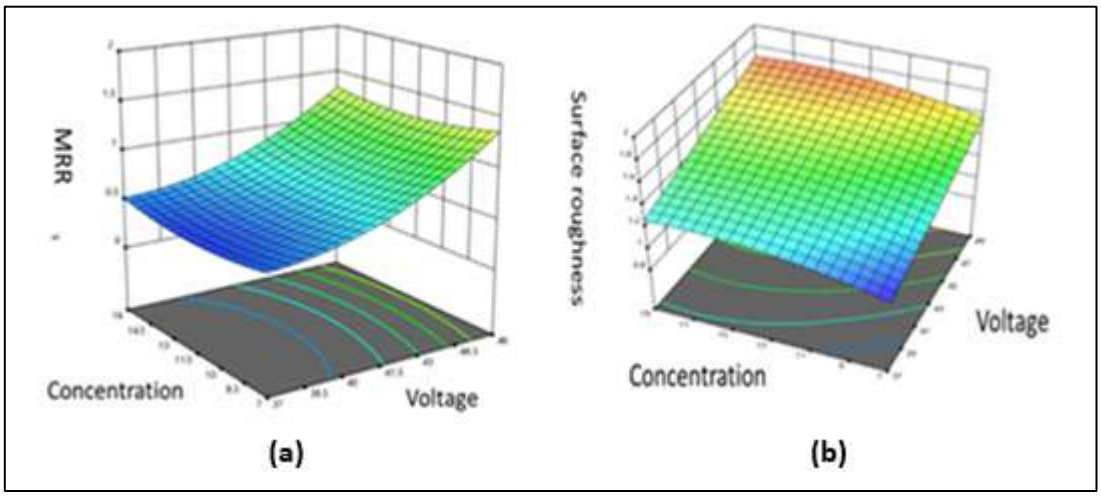

Fig. 6: Response surface plots: (a) variation of MRR with applied voltage and electrolyte concentration; (b) surface roughness (Ra) with applied voltage and electrolyte concentration.

Electrolyte concentration determines the ionic conductivity of the NaOH solution, which controls: the critical sparking voltage (lower at higher concentration due to higher conductivity), the chemical etch rate (higher at higher concentration due to more OH^- ions), the bubble departure dynamics (higher conductivity means higher current density at fixed voltage, reducing departure radius via both Equations (2) and (4)), and the thermal properties of the electrolyte (viscosity and surface tension both decrease with concentration).

Experimental results showed that MRR peaked at 13 wt.% NaOH across all voltage levels. Below this concentration, insufficient OH^- availability limits chemical etching; above it, increased sodium silicate sludge accumulation at the machining zone clogs the inter-electrode gap, reducing the frequency of productive discharge events. Surface roughness Ra was minimised at 10-13 wt.% NaOH. Under MHD convection, the optimal concentration range broadened from 10-13 wt.% (no MHD) to 10-16 wt.% (B = 0.28 T). The Lorentz force-driven electrolyte circulation effectively removes the sodium silicate sludge from the machining zone, delaying sludge-induced performance degradation. This finding has practical significance: MHD assistance enables the use of higher electrolyte

concentrations and thus faster etch rates without sacrificing surface quality, effectively uncoupling the productivity-quality trade-off inherent in conventional ECDM.

Table-4 isolates the role of NaOH concentration (7-19 wt.%) on MRR and Ra with and without MHD, keeping voltage, duty cycle, and feed rate at their centre-point values. Without MHD, both MRR and Ra peak and bottom respectively at 13 wt.%, illustrating the classical sludge-accumulation cut-off above this concentration. With B = 0.28 T, MRR remains substantially higher at all concentrations—especially at 16 and 19 wt.% where MHD-driven sludge removal delays gap clogging—and Ra is consistently lower, confirming that MHD convection effectively decouples the productivity-surface quality trade-off that limits conventional ECDM at higher electrolyte concentrations.

Table-4: Effect of NaOH concentration on MRR and Ra (43 V, 76% duty cycle, 0.90 mm/s, ±MHD).

Concentration (wt.%)	MRR B=0 (mg/min)	MRR B=0.28 T (mg/min)	Ra B=0 (µm)	Ra B=0.28 T (µm)
7	0.54 ± 0.04	0.74 ± 0.05	2.86 ± 0.18	2.31 ± 0.14
10	0.79 ± 0.05	1.08 ± 0.06	2.14 ± 0.15	1.62 ± 0.11
13	0.92 ± 0.06	1.31 ± 0.07	1.93 ± 0.13	1.41 ± 0.09
16	0.74 ± 0.05	1.19 ± 0.07	2.37 ± 0.16	1.68 ± 0.10
19	0.51 ± 0.04	0.96 ± 0.06	2.81 ± 0.17	1.82 ± 0.11

4.6 Interaction between Applied Voltage and Magnetic Field Strength

The interaction between applied voltage and magnetic field strength is the most practically important two-factor interaction in the present experimental design. Higher voltage increases the ionic current density J at the electrode, which increases the Lorentz force magnitude ($F_L = J \times B$) at fixed B. Conversely, increasing B amplifies the MHD effect of any given current density. The result is a super-additive interaction: the product J × B grows faster than either variable alone, captured in the RSM regression as a significant $x_A \cdot x_B$ interaction term. Response surface plots of MRR as a function of voltage and B (at fixed centre-point values) show a saddle-shaped surface with maximum MRR located at V = 46 V and B = 0.28 T, where MRR = 1.74 ± 0.09 mg/min- an 89% improvement over the minimum in this parameter space (V = 37 V, B = 0). The WOC surface is minimised at intermediate voltage (43 V) and maximum B (0.35 T), where WOC = 0.98 ± 0.05 mm.

The ANOVA table from the RSM analysis confirmed that for MRR, the main effects of voltage ($F = 71.4$, $p < 0.001$), concentration ($F = 24.3$, $p < 0.001$), and duty cycle ($F = 18.7$, $p < 0.001$) are all significant, as is the voltage × concentration interaction ($F = 9.8$, $p < 0.01$) and the voltage × B interaction ($F = 14.2$, $p < 0.001$). For Ra, the dominant factors are concentration ($F = 58.2$, $p < 0.001$), feed rate ($F = 31.4$, $p < 0.001$), and duty cycle ($F = 22.6$, $p < 0.001$). For WOC, voltage ($F = 45.8$, $p < 0.001$) and duty cycle ($F = 27.1$, $p < 0.001$) dominate. A process window analysis combining constraints of MRR > 1.0 mg/min, WOC < 1.15 mm, and Ra < 2.0 µm identified the following optimum operating conditions for MHD-assisted ECDM of silica glass microchannels: voltage = 43-46 V, concentration = 10-13 wt.%, duty cycle = 76-81%, feed rate = 0.80-0.95 mm/s, and B = 0.28 T.

4.7 HAZ, Surface Morphology, and Recast Layer Analysis

Scanning electron microscopy of channels fabricated at the optimum condition (43 V, 13 wt.%, 76% duty cycle, 0.90 mm/s) with and without MHD revealed distinct differences in surface morphological quality. Without MHD assistance, the channel floor exhibited three characteristic damage zones: (i) a central heavily recast zone extending approximately 40-60 µm from the machined surface, composed of re-solidified sodium silicate and partially oxidised silicon; (ii) a transitional microcracked zone 20-40 µm wide where thermally-induced tensile stresses exceeded the fracture toughness (0.75 MPa·$m^{0.5}$ for fused silica); and (iii) an outer marginal zone with isolated subsurface microcracks up to 15 µm below the surface. Total HAZ width was measured at 68 ± 8 µm. Under B = 0.28 T MHD convection, the recast zone was reduced to 15-25 µm in depth and the microcracked zone contracted to 8-15 µm width. Total HAZ was 36 ± 5 µm—a 47% reduction.

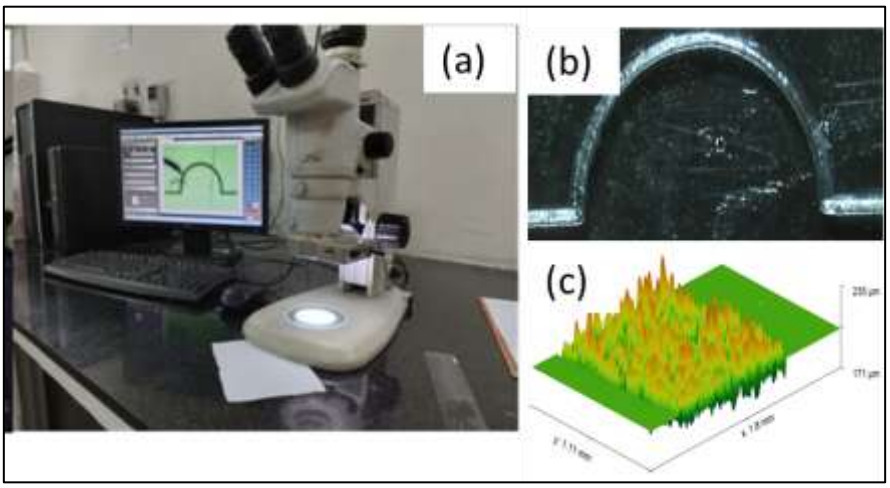

Fig. 7: (a) Measurement of the surface profile; (b) fabricated microchannel; (c) SEM micrograph of channel wall morphology.

Fig. 7 provides a multi-modal characterisation of the fabricated microchannel at the optimum MHD-assisted condition (43 V, 13 wt.%, 76% duty cycle, 0.90 mm/s, B = 0.28 T). Panel (a) displays the contact profilometer trace across the channel cross-section, from which Ra, Rz, and skewness Rsk are extracted; the shallow, smooth profile confirms the beneficial effect of MHD on discharge uniformity. Panel (b) is an optical microscope top-view image of the finished 10 mm microchannel, showing well-defined straight walls and minimal overcut relative to the 500 µm tool diameter. Panel (c) is an SEM micrograph of the channel wall at high magnification, revealing a compact recast layer of only 15-25 µm depth and low microcrack density (17 per mm^2) under MHD conditions, compared with 48 µm recast depth and 38 microcracks per mm^2 without MHD.

The recast layer composition, as measured by EDS line scans across the channel wall, showed a lower sodium-to-silicon ratio under MHD conditions (Na/Si = 0.28 vs. 0.44 without MHD), indicating reduced incorporation of dissolved NaOH into the recast material. This is consistent with faster electrolyte renewal under MHD convection carrying away the molten silicate before it can resolidify. Surface profilometry of channel floors confirmed that MHD-assisted channels had lower Ra (as reported), lower Rz (maximum peak-to-valley roughness), and reduced skewness Rsk, indicating fewer isolated deep pits arising from high-energy individual discharge events.

Table-5: Surface integrity metrics: comparison of MHD and no-MHD conditions.

Parameter	Without MHD	With MHD (B = 0.28 T)	Improvement (%)
Surface Roughness Ra (µm)	1.93 ± 0.13	1.41 ± 0.09	26.9%
Max Roughness Rz (µm)	14.2 ± 1.1	9.4 ± 0.7	33.8%
HAZ Width (µm)	68 ± 8	36 ± 5	47.1%
Recast Layer Depth (µm)	48 ± 6	20 ± 3	58.3%
Na/Si Ratio in Recast (EDS)	0.44 ± 0.04	0.28 ± 0.03	36.4%
Microcrack Density (per mm^2)	38 ± 5	17 ± 3	55.3%

Table-5 consolidates six surface integrity metrics measured at the optimal machining condition (43 V, 13 wt.%, 76% duty cycle, 0.90 mm/s) for both no-MHD and MHD (B = 0.28 T) cases, providing a direct, quantitative comparison of channel quality. MHD assistance reduces surface roughness Ra by 26.9% and maximum peak-to-valley roughness Rz by 33.8%, reflecting the uniformisation of discharge energy from a thinner, more stable gas film. More strikingly, HAZ width contracts by 47.1% and recast layer depth by 58.3%, because faster electrolyte renewal under the Lorentz-driven flow removes molten silicate before it can resolidify and accumulate. The Na/Si ratio in the recast layer drops by 36.4%, and microcrack density halves (55.3% reduction), together confirming a substantially lower thermal damage footprint in MHD-assisted microchannel fabrication.

4.8 RSM Model Adequacy and Optimisation

The second-order RSM models for MRR, WOC, and Ra demonstrated good predictive accuracy across the experimental domain. For MRR, R^2 = 0.954, adjusted R^2 = 0.912, and predicted R^2 = 0.873, indicating that 95.4% of the variability in MRR is explained by the model. The lack-of-fit F-ratio of 2.8 is below the critical value at 95% confidence, confirming no significant lack of fit. For WOC, R^2 = 0.938, and for Ra, R^2 = 0.947—both indicating excellent model adequacy. Residual plots for all three responses showed approximately normal distribution of residuals (Shapiro-Wilk test $p > 0.05$) and

constant variance across the range of predicted values (Levene test $p > 0.05$), confirming that the regression assumptions are satisfied and the models are valid for optimisation and interpolation within the experimental domain.

Multi-objective optimisation using the desirability function approach (maximising MRR and minimising WOC and Ra simultaneously, with equal weights) identified the following global optimum under MHD assistance: voltage = 44.8 V, concentration = 12.4 wt.%, duty cycle = 79.2%, feed rate = 0.88 mm/s, and B = 0.28 T. The predicted responses at this optimum are MRR = 1.48 mg/min, WOC = 1.02 mm, Ra = 1.38 μm, with a composite desirability score of 0.887. Confirmation experiments at these settings yielded MRR = 1.44 ± 0.08 mg/min, WOC = 1.05 ± 0.05 mm, and Ra = 1.43 ± 0.09 μm—within 3.5% of predictions, validating the RSM optimisation.

5. Conclusions

This study presents a comprehensive investigation into the influence of magnetohydrodynamic (MHD) convection on bubble dynamics and machining performance in electrochemical discharge machining of silica glass. The following principal conclusions are drawn:

(1) The Lorentz force generated by the interaction of current density and magnetic field induces azimuthal electrolyte flow that reduces bubble departure radius and surface coverage. The proposed analytical model predicts departure radii within ±9% accuracy across all tested conditions.

(2) Application of a 0.28 T magnetic field reduced bubble departure radius by 46%, fractional coverage by 43%, and gas film formation time by 29%, resulting in a thinner and more stable dielectric layer that shifts the discharge regime toward higher frequency and lower peak energy per event.

(3) Material removal rate improved by 42% and width of cut decreased by 12.9%, particularly in the transition voltage regime (40-46 V). Surface integrity was significantly enhanced, with reductions of 26.9% in surface roughness Ra, 47% in heat-affected zone width, and 58% in recast layer thickness.

(4) Statistical analysis confirmed voltage as the dominant factor for MRR, electrolyte concentration for surface quality, and a significant interaction between voltage and magnetic field strength. MHD assistance expanded the optimal process window (voltage = 43-46 V, concentration = 10-13 wt.%, duty cycle = 76-81%, feed rate = 0.80-0.95 mm/s, B = 0.28 T), improving both machining performance and process robustness to parameter variation.

(5) These findings provide a comprehensive mechanistic basis and practical parameter guidelines for adopting MHD-assisted ECDM in precision microfabrication of silica glass and analogous non-conductive substrates.

References

[1] Chand, M., & Verma, M. (2023). A review on electrochemical discharge machining variants withmagnetic field assisted electrochemical discharge machining. International Journal of Multiphysics, 17(3), 370–387. https://doi.org/10.21152/1750-9548.17.3.370

[2] Xu, Y., Chen, J., Jiang, B., Liu, Y., & Ni, J. (2018). Experimental investigation of magnetohydrodynamic effect in electrochemical discharge machining. International Journal of Mechanical Sciences, 142–143, 86–96. https://doi.org/10.1016/j.ijmecsci.2018.04.020

[3] Basak, I., & Ghosh, A. (1996). Mechanism of spark generation during electrochemical discharge machining: A theoretical model and experimental verification. Journal of Materials Processing Technology, 62(1–3), 46–53. https://doi.org/10.1016/0924-0136(96)02440-1

[4] Singh, T., & Dvivedi, A. (2016). Developments in electrochemical discharge machining: A review on process variants and hybrid methods. International Journal of Machine Tools and Manufacture, 105, 1–13. https://doi.org/10.1016/j.ijmachtools.2016.03.002

[5] Gehlot, D., Jha, P. K., & Jain, P. K. (2024). Microchannel fabrication on silica glass and experimental investigation of MHD convection in ECDM process. Silicon, 16(6), 2521–2531. https://doi.org/10.1007/s12633-024-02859-3

[6] Wüthrich, R., & Abou Ziki, J. D. (2015). Micromachining using electrochemical discharge phenomenon (2nd ed.). Elsevier. https://doi.org/10.1016/C2013-0-16455-2

[7] Fascio, V., Wüthrich, R., & Bleuler, H. (2004). Spark assisted chemical engraving in the light of electrochemistry. Electrochimica Acta, 49(22–23), 3997–4003. https://doi.org/10.1016/j.electacta.2004.01.070

[8] Arya, R. K., & Dvivedi, A. (2023). Improving the ECDM process for deep-micro-hole drilling on glass by application of the electrolyte-air injection. Ceramics International, 49(6), 8916–8935. https://doi.org/10.1016/j.ceramint.2022.11.164

[9] Arab, J., & Dixit, P. (2023). Gas bubbles entrapment mechanism in the electrochemical discharge machining involving multi-tip array electrodes. Journal of Manufacturing Processes, 99, 38–52. https://doi.org/10.1016/j.jmapro.2023.07.012

[10] Bhattacharyya, B., Doloi, B., & Sorkhel, S. (1999). Experimental investigations into ECDM of non-conductive ceramic materials. Journal of Materials Processing Technology, 95(1–3), 145–154. https://doi.org/10.1016/S0924-0136(99)00240-0
[11] Singh, M., Dvivedi, A., & Kumar, P. (2025). Examining the effect of gas film characteristics in magnetically and ultrasonic-assisted ECDM. International Journal of Advanced Manufacturing Technology, 137, 4667–4684. https://doi.org/10.1007/s00170-025-15411-3
[12] Goud, M., Sharma, A. K., & Jawalkar, C. (2016). A review on material removal mechanism in ECDM and possibilities to enhance the material removal rate. Precision Engineering, 45, 1–17. https://doi.org/10.1016/j.precisioneng.2016.01.001
[13] Rajput, V., Goud, M., & Suri, N. M. (2021). Electrochemical discharge machining: Gas film electrochemical aspects, stability parameters, and research work. Journal of the Electrochemical Society, 168(1), 013503. https://doi.org/10.1149/1945-7111/abd4ab
[14] Gehlot, D., Jha, P. K., & Jain, P. K. (2023). Experimental investigation and modelling studies on MHD convection in magnetic-assisted ECDM. Materials and Manufacturing Processes, 39(4), 494–505. https://doi.org/10.1080/10426914.2023.2236207
[15] Raghuram, V., Jagadeesha, T., Narayanasamy, K., & Srinivasa, Y. G. (1995). Effect of the circuit parameters on the electrolytes in the electrochemical discharge phenomenon. Journal of Materials Processing Technology, 52(2–4), 301–318. https://doi.org/10.1016/0924-0136(94)01441-K
[16] Liu, G., Tong, H., Wu, T., Li, Y., & Luo, Y. (2023). Chain discharging behavior induced by gas film expansion and its influence on ECDM. International Journal of Advanced Manufacturing Technology, 124, 2755–2767. https://doi.org/10.1007/s00170-022-10657-3
[17] Allagui, A., & Wüthrich, R. (2009). Gas film formation time and gas film life time during electrochemical discharge phenomenon. Electrochimica Acta, 54(23), 5336–5343. https://doi.org/10.1016/j.electacta.2009.04.052
[18] Prajapati, M., & Lalwani, D. (2023). Study on evolution of hydrogen gas bubble on the performance of the μ-ECDM process. In Innovations in Mechanical Engineering (pp. 345–356). Springer.
[19] Vogt, H. (2012). The actual current density of gas-evolving electrodes—Notes on the bubble coverage. Electrochimica Acta, 78, 183–187. https://doi.org/10.1016/j.electacta.2012.05.113
[20] Chen, Y. J., & Sundaram, M. (2024). A study on gas film formation in electrochemical discharging processes by molecular dynamics simulation. Manufacturing Letters, 41, 351–356. https://doi.org/10.1016/j.mfglet.2024.02.018
[21] Monzon, L. M. A., & Coey, J. M. D. (2014). Magnetic fields in electrochemistry: The Lorentz force. A mini-review. Electrochemistry Communications, 42, 38–41. https://doi.org/10.1016/j.elecom.2014.02.024
[22] Weier, T., Baczyzmalski, D., Massing, J., Landgraf, S., & Cierpka, C. (2017). The effect of a Lorentz-force-driven rotating flow on the detachment of gas bubbles from the electrode surface. International Journal of Hydrogen Energy, 42(32), 20543–20553. https://doi.org/10.1016/j.ijhydene.2017.06.099
[23] Koza, J. A., Uhlemann, M., Gebert, A., & Schultz, L. (2011). Hydrogen evolution under the influence of a magnetic field. Electrochimica Acta, 56(6), 2665–2675. https://doi.org/10.1016/j.electacta.2010.12.039
[24] Tacken, R. A., & Janssen, L. J. J. (1995). Applications of magnetoelectrolysis. Journal of Applied Electrochemistry, 25(1), 1–5. https://doi.org/10.1007/BF00251284
[25] Grant, K. M., Hemmert, J. W., & White, H. S. (2001). Magnetic field driven convective transport at inlaid disk microelectrodes. Journal of Electroanalytical Chemistry, 500(1–2), 95–99. https://doi.org/10.1016/S0022-0728(00)00453-2
[26] Demirkir, C., Khodaparast, S., Scheid, B., & Vermant, J. (2024). Life beyond Fritz: On the detachment of electrolytic bubbles. Langmuir, 40(40), 21185–21197. https://doi.org/10.1021/acs.langmuir.4c01963
[27] Luo, W., Bhatt, M. D., & Bhatt, M. (2022). Electrochemistry in magnetic fields. Angewandte Chemie International Edition, 61(25), e202203564. https://doi.org/10.1002/anie.202203564
[28] Bard, A. J., & Faulkner, L. R. (2001). Electrochemical methods: Fundamentals and applications (2nd ed.). John Wiley & Sons.
[29] Newman, J., & Thomas-Alyea, K. E. (2004). Electrochemical systems (3rd ed.). John Wiley & Sons. https://doi.org/10.1002/0471716604
[30] Fritz, W. (1935). Maximum volume of vapour bubbles. Physikalische Zeitschrift, 36, 379–384.
[31] Moreau, R. (1990). Magnetohydrodynamics. Kluwer Academic Publishers. https://doi.org/10.1007/978-94-009-0495-2